Materials Today Advances 16 (2022) 100280

Contents lists available at ScienceDirect

Materials Today Advances

journal homepage: www.journals.elsevier.com/materials-today-advances/

# Strategy to weaken the oxygen adsorption on single-atom catalysts towards oxygen-involved reactions

Chengyi Zhang [a, 1], Yuhang Dai [b, c, 1], Qi Sun [b], Chumei Ye [d], Ruihu Lu [b, **], Yazhou Zhou [e, f, ***], Yan Zhao [a, b, *]

[a] Institute of Technological Sciences, Wuhan University, Hubei, Wuhan, 430072, People's Republic of China
[b] State Key Laboratory of Advanced Technology for Materials Synthesis and Processing, Wuhan University of Technology, Wuhan, 430070, PR China
[c] Christopher Ingold Laboratory, Department of Chemistry, University College London, London, WC1H 0AJ, United Kingdom
[d] Department of Materials Science and Metallurgy, University of Cambridge, Cambridge, CB3 0FS, United Kingdom
[e] School of Materials Science and Engineering, Jiangsu University, Zhenjiang, Jiangsu, 212013, People's Republic of China
[f] Max Planck Institute for Polymer Research, 55128, Mainz, Germany

ARTICLE INFO

*Article history:*
Received 30 June 2022
Received in revised form
7 August 2022
Accepted 9 August 2022
Available online xxx

*Keywords:*
Single-atom catalyst
Oxygen reactions
Density functional theory
Axial coordination

ABSTRACT

Single-atom catalysts (SACs) are promising for 4e⁻oxygen reduction reaction (4e⁻ORR). However, they are rarely utilized in other oxygen-involved reactions, e.g. 2e⁻ORR to produce $H_2O_2$, 4e⁻oxygen evolution reaction (4e⁻OER), and 2e⁻water oxidation reaction (2e⁻WOR). Herein, we applied density functional theory (DFT) calculations to investigate the applicabilities of SACs, including Ti, V, Cr, Mn, Fe, Co, Ni, Cu, Zn, Nb, Mo, Ru, Rh, Pd, Pt, and Au with axial coordination (e,g, −OH, =O, and ≡N) for all 4e⁻/2e⁻ oxygen reactions. With axial coordination, SACs derived from early transition metals exhibit high catalytic performance, including V-SAC-OH with an overpotential of 0.61 V for 4e⁻ORR, Mo-SAC-OH with an overpotential of 0.05 V for 2e⁻ORR, Mo-SAC-O with an overpotential of 0.52 V for 4e⁻OER, and Nb-SAC-OH with an overpotential of 0.14 V for 2e⁻WOR. Among them, most SACs deliver a trend of adsorption-energy decreasing with the increase of axial bond, which successively meets various adsorption requirements of all 4e⁻/2e⁻ oxygen reactions. This finding has led to the discovery of highly active SACs adapted to different oxygen reactions. Importantly, an intrinsic framework that combines SAC configuration, transition metal (TM) species, and TM charges was established to describe the adsorption ability of SACs. This work offers an intrinsic landscape to understand the correlation of the adsorption ability of SACs with the tendentiousness of oxygen-involved reactions and guides the rational design of SACs.

© 2022 The Authors. Published by Elsevier Ltd. This is an open access article under the CC BY-NC-ND license (http://creativecommons.org/licenses/by-nc-nd/4.0/).

## 1. Introduction

Oxygen-involved electrocatalytic reactions, including 4e⁻/2e⁻oxygen reduction reaction (ORR), 4e⁻oxygen evolution reaction (OER), and 2e⁻water oxidation reaction (WOR), are key reactions for new-generation energy technologies utilizing renewable clean fuels [1–3]. Up to now, tremendous effort has been devoted to the discovery and design of advanced electrocatalysts, such as transition metal/alloys [4], sulfides [5], phosphides [6], oxides [7,8], (Oxy) hydroxides [9], and carbon-based materials [10]. Among them, precious metal materials, mainly platinum-group metals [11,12], are the only commercially available catalysts, but their high costs and scarcity severely inhibit their large-scale commercial applications. Designing non-precious metal catalysts with high oxygen electrocatalytic performance to replace noble-metal-based catalysts is essential for practical applications.

Single-atom catalysts (SACs) can be obtained by anchoring the single transition metal (TM) atom on nitrogen-doped carbon materials [13–17], and have been employed in oxygen-involving reactions. The active centers of SACs are mainly tetracoordinate

* Corresponding author. Institute of Technological Sciences, Wuhan University, Hubei, Wuhan, 430072, People's Republic of China.
** Corresponding author.
*** Corresponding author. School of Materials Science and Engineering, Jiangsu University, Zhenjiang, Jiangsu, 212013, People's Republic of China.
*E-mail addresses:* ruihulu@whut.edu.cn (R. Lu), yazhou@mpip-mainz.mpg.de (Y. Zhou), yan2000@whut.edu.cn (Y. Zhao).
[1] These authors contributed equally to this work. C. Z and R. L conceived and supervised the project. C. Z, Y. D, C, Y, and R. L complete the original idea. C. Z and R. L interpreted the results and wrote the manuscript; Y. Z, Q. S, and Y. Z supervised these theoretical simulations; All authors have contributed to the scientific discussion of the project.

https://doi.org/10.1016/j.mtadv.2022.100280
2590-0498/© 2022 The Authors. Published by Elsevier Ltd. This is an open access article under the CC BY-NC-ND license (http://creativecommons.org/licenses/by-nc-nd/4.0/).

planar TM-$N_4$ moieties, and some SACs (e.g., Mn, Fe, Co, Ni, and Cu) can efficiently catalyze oxygen reactions [18–23]. For example, Fe-based SACs favor ORR, while Co-based SACs tend to catalyze $O_2$ into $H_2O_2$ [24,25]. Nevertheless, other SACs, especially those that originated from early TMs, generally exhibit extremely poor performance due to their relatively excessive adsorption strengths [26].

In this work, to effectively reduce the adsorption strength of single-atom catalysts, we tune strong axial coordination (-OH, =O, and ≡N) to SACs for tailoring the adsorption ability of TM-derived SACs. Using density functional theory (DFT) calculations, we systematically investigated the role of axial coordination in regulating $O_2$ adsorption and catalytic performance on various SACs. Our results revealed that many SACs, not reported yet, exhibited exceptionally good activity for $4e^-/2e^-$ oxygen reactions, including V-SAC-OH with an overpotential of 0.61 V for $4e^-$ORR, Mo-SAC-OH with an overpotential of 0.05 V for $2e^-$ORR, Mo-SAC-O with an overpotential of 0.52 V for $4e^-$OER, and Nb-SAC-OH with an overpotential of 0.14 V for $2e^-$WOR. Herein, we demonstrated that weakening the adsorption ability of SACs towards oxygenated species (*OOH, *OH, and *O) can promote the catalytic activity toward different oxygen-involved reactions. Furthermore, we proposed a theoretical framework that integrates the SAC configuration, TM species, and TM charges to describe the catalytic ability of SACs. Our results built a full profile to understand the catalytic behavior of SACs and provided a new approach for developing highly active SACs in oxygen-involved reactions.

## 2. Computational details

All spin-polarized [27] DFT calculations were conducted with the Vienna *Ab initio* simulation package (VASP) [28,29]. The exchange-correlation functional was described by the popular Perdew-Burke-Ernzerhof (PBE) generalized gradient approximation (GGA) [30]. The frozen-core projector-augmented wave (PAW) method with a cutoff energy of 520 eV was used to describe the interaction between core electrons and valence electrons [31]. In addition, Grimme's DFT-D3 scheme was used to describe the long-range vdW interactions [32]. A $6 \times 6 \times 1$ supercell of graphene layer embedded with The TM-$N_4$ moiety was embedded in a $6 \times 6 \times 1$ supercell of graphene layer to simulate the TM-SAC catalyst. A 15 Å vacuum layer was set to eliminate the interactions with the periodic images along the Z axial direction. $\Gamma$-centred Monkhorst–Pack *k*-point mesh grid of $3 \times 3 \times 1$ was employed for all supercells [33]. Moreover, the criteria of energy and force convergence were set to $1.0 \times 10^{-5}$ eV per atom and 0.02 eV $Å^{-1}$ for geometry optimization, respectively. Bader charge analysis was used to study the atomic charge changes. The VESTA program [34] was employed to construct all models and to plot charge density differences.

The elementary steps for $4e^-$ORR in an acidic medium are shown in Eqs (1)–(4), whereas the elementary steps for $2e^-$ORR to produce $H_2O_2$ are the combination of Eqs (1) and (5).

$$* + O_2 + H^+ + e^- \rightarrow *OOH \quad (1)$$

$$*OOH + H^+ + e^- \rightarrow *O + H_2O \quad (2)$$

$$*O + H^+ + e^- \rightarrow *OH \quad (3)$$

$$*OH + H^+ + e^- \rightarrow * + H_2O \quad (4)$$

$$*OOH + H^+ + e^- \rightarrow * + H_2O_2 \quad (5)$$

The $4e^-$OER pathway is shown in Eqs (6)–(9), and the $2e^-$WOR pathway to form $H_2O_2$ is the combination of Eqs (6) and (10).

$$* + H_2O \rightarrow *OH + H^+ + e^- \quad (6)$$

$$*OH \rightarrow *O + H^+ + e^- \quad (7)$$

$$*O + H_2O \rightarrow *OOH + H^+ + e^- \quad (8)$$

$$*OOH \rightarrow * + O_2 + H^+ + e^- \quad (9)$$

$$*OH + H_2O \rightarrow * + H_2O_2 + H^+ + e^- \quad (10)$$

where * denote adsorbed sites on SACs, adsorbed intermediates *OOH, *O, and *OH are adsorbed intermediates, respectively.

For each elemental step, the Gibbs free energy $\Delta G_i$ can be calculated using Eq (11).

$$\Delta G = \Delta E + \Delta E_{ZPE} - T\Delta S + \Delta G_{pH} + \Delta G_U \quad (11)$$

where $\Delta E$ is the total energy of reactions obtained from DFT calculations, $\Delta E_{ZPE}$ and $\Delta S$ represent the changes of zero-point energy and entropy, respectively. $T$ denotes the temperature (298.15 K). The zero-point energy and entropy are calculated using the vibrational frequencies of the oxygenated intermediate species based on the harmonic normal mode approximation while fixing the catalyst slab. $\Delta G_{pH} = -k_B T \ln[H^+] = k_B \times pH \times \ln 10$ is the contribution of $H^+$ concentration change for Gibbs free energy during the ORR process, where $k_B$ is the Boltzmann constant, and the value of pH is assumed to be zero. $\Delta G_U = -neU$ is the contribution of applied electrode potential, where $n$ is the number of electrons transferred in each elemental reaction and $U$ is the applied electrode potential. Besides, according to the computational hydrogen electrode (CHE) model suggested by Nørskov et al. [35,36], the chemical potential of a proton/electron pair is equal to half of the energy of $H_2$. Due to the difficulties in the DFT calculations of open-shell triplet $O_2$, the free energy of the $O_2$(g) molecule is calculated by $G_{O_2(g)} = 2G_{H_2O} - 2G_{H_2} + 4.92$ eV [35].

Based on the free energies of elemental steps, the thermodynamic overpotential of ORR/OER/WOR on SACs can be obtained via Eqs (12)–(15). The elementary step with the maximum overpotential is considered the potential-determining step (PDS), which limits the ORR/OER/WOR processes.

$$\eta^{4e^- ORR} = max\{\Delta G_1, \Delta G_2, \Delta G_3, \Delta G_4\} / e + 1.23\ V \quad (12)$$

$$\eta^{2e^- ORR} = max\{\Delta G_1, \Delta G_5\} / e + 0.68\ V \quad (13)$$

$$\eta^{4e^- OER} = max\{\Delta G_6, \Delta G_7, \Delta G_8, \Delta G_9\} / e - 1.23\ V \quad (14)$$

$$\eta^{2e^- WOR} = max\{\Delta G_6, \Delta G_{10}\} / e - 1.78\ V \quad (15)$$

Eqs (16)–(18) are the reactions for the formations of key intermediates on SACs.

$$* + 2H_2O \rightarrow *OOH + 3/2H_2 \quad (16)$$

$$* + H_2O \rightarrow *O + H_2 \quad (17)$$

$$* + H_2O \rightarrow *OH + 1/2H_2 \quad (18)$$

The calculated free energy of formation of each key ORR-intermediate can be obtained by using Eqs (19)–(21):

$$\Delta G_{*OOH} = G_{*OOH} + 3/2G_{H_2} - G_* - 2G_{H_2O} \quad (19)$$

$$\Delta G_{*O} = G_{*O} + G_{H_2} - G_* - G_{H_2O} \quad (20)$$

$$\Delta G_{*OH} = G_{*OH} + 1/2\,G_{H_2} - G_* - G_{H_2O} \quad (21)$$

## 3. Results and discussion

### 3.1. $O_2$ adsorption on SACs

Experimentally, TMs can be embedded into the bulk vacancies such as single vacancy, double vacancies, and Stone-Wales defects [37], to form single-atomic active sites. It is observed that most of the metals are trapped at the nitrogenated double vacancies based on the advanced characterization including transmission electron microscopy and X-ray absorption near edge structure [23,38], displayed in Fig. 1(a), and it is the SAC model in this study. A total of 18 metals, including all 3*d* TMs except Sc, six 4*d* TMs, and three 5*d* TMs can be anchored on N-doped graphene via chemically binding with four pyridinic-nitrogen atoms (Figs. S1–2). Due to their lone-pair orbitals, we choose axial ligands (e.g., –OH, =O, and ≡N) to strongly bound to the central metals of these SACs (Fig. S3) via single-, double-, and triple-bonds, respectively, in Fig. 1(b). Increasing the axially coordinated orbitals with d orbitals can gradually increase the interaction with central metals of SACs. In addition, the dissolution potential in Fig. S4 shows that SACs with axial ligands exhibit higher stability in an electro-chemical environment. Finally, 72 SACs were screened for further investigation.

Theoretically, $O_2$ adsorption/desorption is a key process for ORR/OER, reflecting the reactivity of SACs. We thus estimated the $O_2$ adsorption ability on SACs through $O_2$ adsorption energy and configuration. Fig. 1(c) demonstrated four adsorption configurations of $O_2$ molecules, including dissociation adsorption **$O_{2ad}$ (1)**, side-on adsorption **$O_{2ad}$ (2)**, top-on adsorption **$O_{2ad}$ (3)**, and physisorption **$O_{2ad}$ (4)**. These configurations of $O_2$ adsorption highly correlate with the interaction between oxygen molecules and active sites [39], revealing the change in the adsorption ability of SACs.

We then optimized $O_2$ adsorption on SACs. Our computations in Fig. 1(d) demonstrated that SACs derived from early TMs strongly adsorb $O_2$ and form the **$O_{2ad}$ (2)** configuration with stretched $O_2$ bonding length. This indicates that these early TMs delivered a high adsorption ability towards $O_2$. SACs derived from late TMs show relatively weak adsorption ability with the **$O_{2ad}$ (3)** or **$O_{2ad}$ (4)** configuration. With the axial ligands being stronger, the $O_2$ adsorption configuration gradually changes from **$O_{2ad}$ (2)** to **$O_{2ad}$ (4)**, especially for Ti, V, Nb, and Mo. Besides, the corresponding O–O binding length and adsorption energy decrease with stronger ligand bonding as displayed in Figs. S5 and S6. Hence, axial coordination was confirmed to effectively regulate the adsorption of SACs for further investigation in oxygen reactions.

### 3.2. Catalytic activity of SACs

The intrinsic catalytic activity of SACs with axial ligands towards

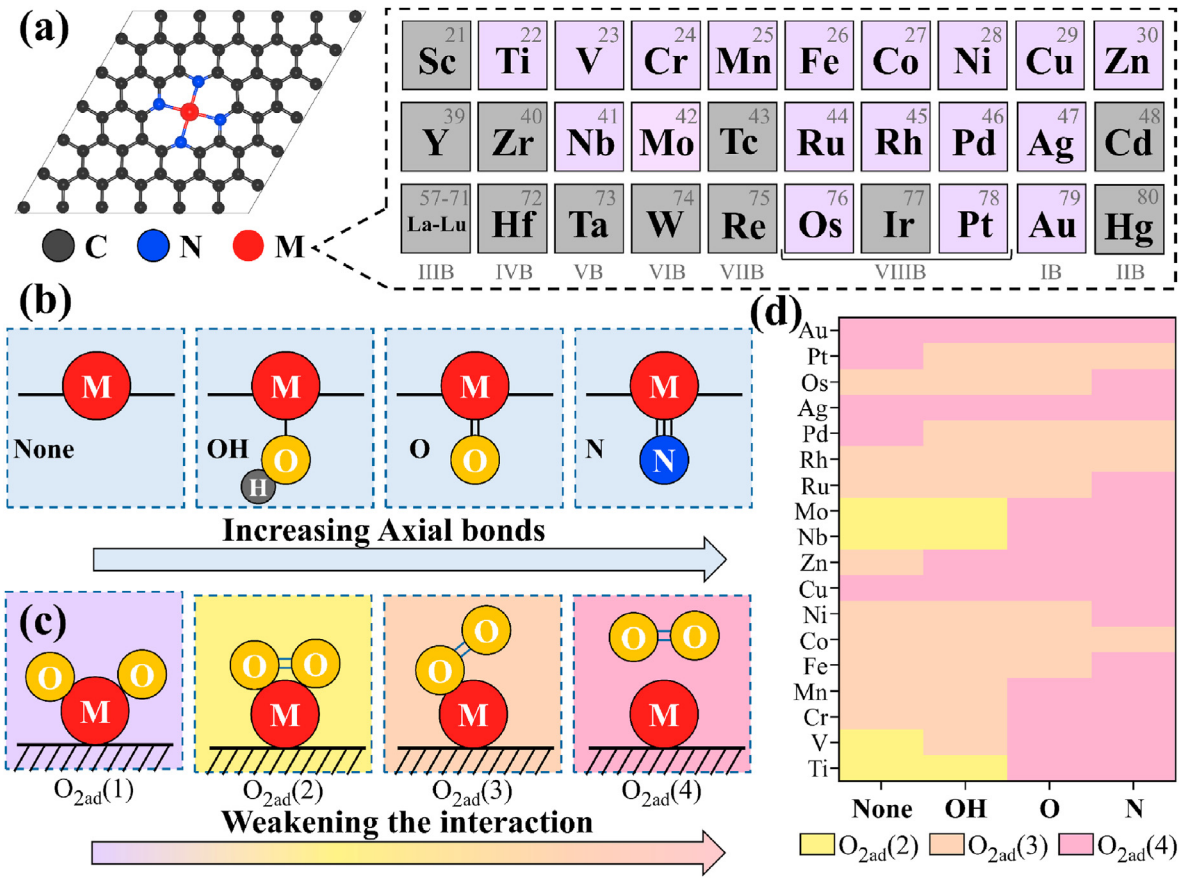


**Fig. 1.** Structural prototype of SACs (**a**). The axial ligand-free SAC and SACs with OH, O, and N axial ligands (**b**). The possible $O_2$ adsorption configurations on SACs (**c**). The distribution of $O_2$ adsorption configurations on SACs (**d**).

oxygen reaction was further investigated. As exhibited in Fig. 2(a), the 4-electron ORR can be divided into four steps based on the number of electron transfers. Depending on the $O_2$ adsorption configuration, the adsorbed $O_2$ interacted with the first $H^+/e^-$ pair and then generate three different species 1, including *O+*OH, *O*OH, and *OOH. Besides, all these species 1 can expose two oxygen sites for the subsequent hydrogenation. The second $H^+/e^-$ pair can accordingly attack either of the oxygen atoms of species 1 to form species 2, including the intermediates (*OH+*OH or *O) or the production of $H_2O_2$. The generation of $H_2O_2$ implies the completion of 2e$^-$ORR and the start of the next reaction cycle [2]. If the third electron/proton transfer occurs, the above intermediates can only convert into species 3, namely *OH, and then reduced to $H_2O$, followed by desorption. With 4-electron transferred, $O_2$ can be reduced to $H_2O$, which finalizes the 4e$^-$ORR process [40]. Along the reverse direction of electron transfer, the $H_2O$ molecule couples two or four electrons to form $H_2O_2$ and $O_2$, corresponding to 2e$^-$WOR and 4e$^-$OER, respectively [8,41].

Within the theoretical frame of such four oxygen-involving reactions, we calculated the free energy change for each elementary reaction in Eqs (1)–(10) (Tables S3–4). Based on Eqs (12)–(15), we estimated the catalytic activity of SACs (with/without axial coordination) by using the DFT calculated overpotential. Fig. 2(b-e) summarized the heatmaps of the overpotentials on SACs. Taking the 4e$^-$ORR overpotential of 0.43 V on Pt (111) as a golden standard [35], a few SACs even without axial coordination exhibit high catalytic performances such as Cr- and Mn-SAC for 2e$^-$ORR, Co- and Rh-SAC for 4e$^-$ORR, 2e$^-$ORR, and 4e$^-$OER, Ni-, Cu-, Ag-, and Au-SAC for 2e$^-$WOR, Zn-SAC for 4e$^-$OER. None of the SACs derived from the other 11 TMs, especially the early TMs, exhibit low overpotentials for the oxygen-involving reactions, revealing that the late TM metal-derived SACs have a superior catalytic activity compared to the early TM-derived SAC in catalyzing $O_2/H_2O$ conversion [42]. With axial coordination, a large number of newly active SACs arise including 6 SACs for 4e$^-$ORR, 16 SACs for 2e$^-$ORR, and 5 SACs for 4e$^-$OER, and 20 SACs for 2e$^-$WOR. Meanwhile, some SACs possess higher or comparable catalytic performance to the conventional tetra-coordinated SACs: 4 SACs for 4e$^-$ORR, 10 SACs for 2e$^-$ORR, and 6 SAC for 2e$^-$WOR. Especially, Mo-SAC-OH possesses the lowest overpotential of 0.05 V towards 2e$^-$ORR, revealing that the Mo-SAC-OH is a potential excellent catalyst for 2e$^-$ORR. Nb-SAC-OH exhibited the best catalytic activity towards 2e$^-$WOR with the lowest overpotential of 0.01 V. Therefore, it proved again that moderate axial coordination can be an efficient strategy to regulate the catalytic activity of SACs. Furthermore, it is worth noting that early TM-derived SACs display great potential in the development of new catalysts for catalyzing oxygen reactions via axial coordination.

### 3.3. Regulation rule of SACs

The above activity data motivated us to find an underlying mechanism to shed light on the regulation rule for SAC systems. First, we constructed the scaling relation between the adsorption energy of three key intermediates (species 1, 2, and 3) to describe the adsorption behavior of SACs. Apart from *O+*OH on Ti-SAC, V-SAC, Nb-SAC, and Mo-SAC, the adsorption energy of other species 1 (*O*OH and *OOH) linearly correlated with the adsorption energy of *OH with R-square of 0.93 in Fig. 3(a).

The linear relation between $\Delta G_{*OOH}$ and $\Delta G_{*OH}$ is $\Delta G_{*OOH} = 0.87\Delta G_{*OH} + 3.2$. This is similar to the scaling relation: $\Delta G_{*OOH} = \Delta G_{*OH} + 3.2$ in metal oxides [43]. Meanwhile, due to the different bonding patterns in *O/*OH (double-bond vs single-bond) and the high sensitivity of double-bonded *O to the adsorption site,

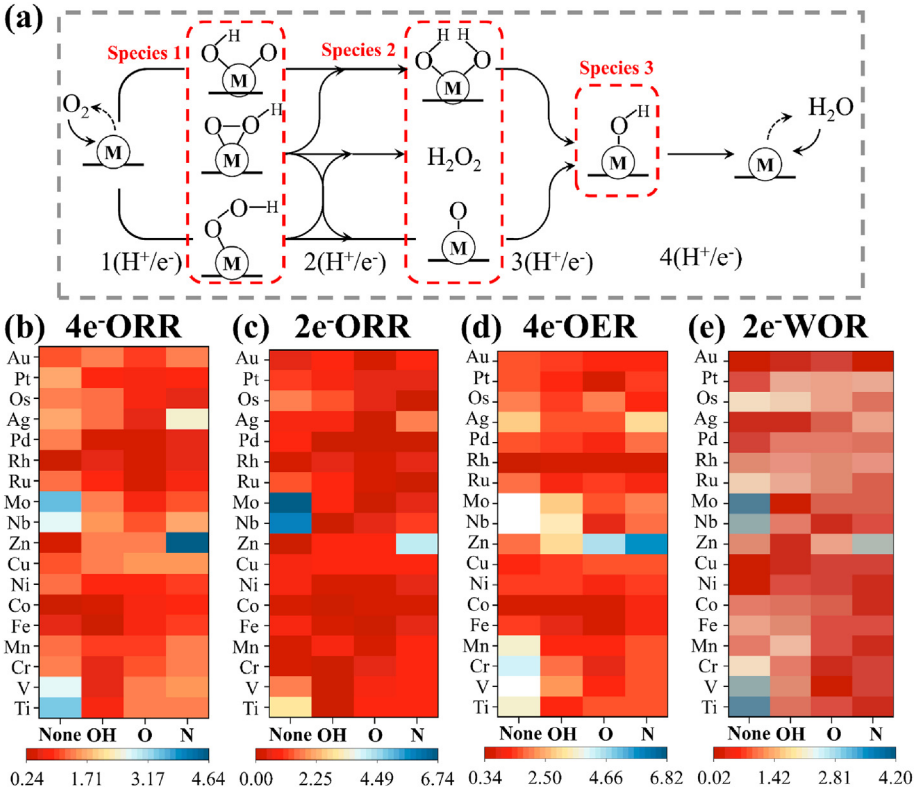


**Fig. 2.** The 4e$^-$/2e$^-$ORR pathways on SACs along with the hydrogen/electron transfer **(a)**. The heatmap of catalytic activity (Overpotential / V) of 4e$^-$ORR **(b)**, 2e$^-$ORR **(c)**, 4e$^-$OER **(d)**, and 2e$^-$WOR **(e)** on various SACs.

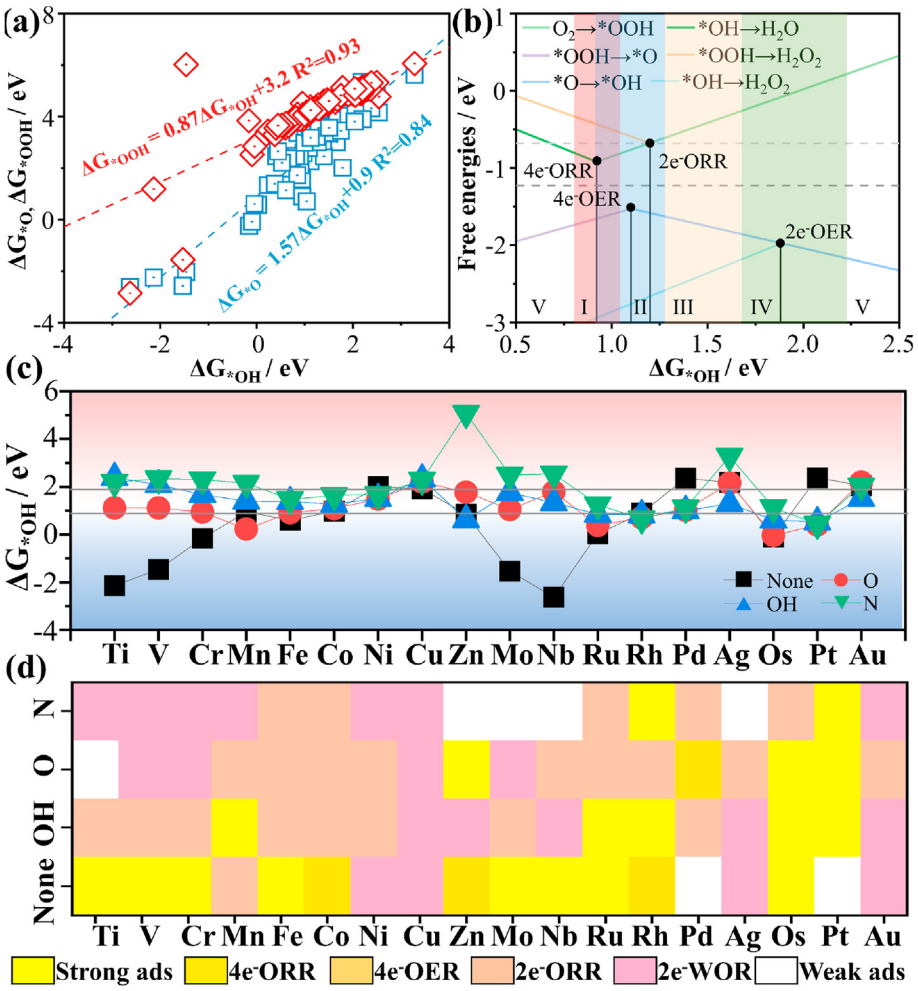


**Fig. 3.** The scaling relation of $\Delta G_{*OH}$ vs. $\Delta G_{*OOH}$ and $\Delta G_{*O}$ **(a)**. The volcano curve of SACs on basis of ORR free energies **(b)**. The I, II, III, IV, and V regions represent the feasible $\Delta G_{*OH}$ ranges for highly 4e⁻ORR, 4e⁻OER, 2e⁻ORR, 2e⁻WOR, and sluggish oxygen reactions. The distribution of *OH adsorption energy of SACs **(c)**. The gray lines denote the optimal *OH adsorption energy for 4e⁻ORR and 2e⁻WOR. The suitable catalytic oxygen reaction of various SACs **(d)**.

the linear relationship for *O/*OH (R-square = 0.84) is not as good as that for *OH/*OOH (R-square = 0.93), and the fitted linear relationship for *O/*OH is: $\Delta G_{*O} = 1.57\Delta G_{*OH} + 0.9$. Accordingly, these linear fitting showed that the adsorption energy of *OH can be employed as a descriptor to describe the influence of the change of adsorption in the catalytic activity. Furthermore, Fig. 3(b) exhibits a volcano-shaped relationship between free energy change along oxygen reactions and the adsorption energy of *OH. The commercial Pt/C has an overpotential of 0.43 V for ORR, and we have used this value to screen the electrocatalysts. It is worth noting in Fig. S7 that there are four volcano peaks corresponding to 4e⁻ORR [44], 4e⁻OER [45], 2e⁻ORR [46], and 2e⁻WOR [41], respectively. The optimal $\Delta G_{*OH}$ is corresponding to 0.92, 1.10, 1.20, and 1.93 eV. It indicates that the high-performance 4e⁻ORR catalysts require relatively strong adsorption, whereas 4e⁻OER, 2e⁻ORR, and 2e⁻WOR require weak $\Delta G_{*OH}$. Fig. S8 demonstrates that weakening *OH adsorption can gradually increase the catalytic activity toward 4e⁻ORR, 4e⁻OER, 2e⁻ORR, and 2e⁻WOR. Fig. 3(c) presents the $\Delta G_{*OH}$ values of conventional SACs, and Ti-, V-, Cr-, Mo-, Nb-, Ru-, and Os-SACs possess strong adsorption with $\Delta G_{*OH}$ below or close to 0 V and are located in area I in Fig. 3(b). This indicated that they have poor catalytic activity towards all oxygen reactions, which is consistent with the previous discussion. Mn-, Fe-, Co-, Ni-, and Rh-SACs exhibited a feasible $\Delta G_{*OH}$ near 1 eV in area II. These SACs deliver good ORR performance [21]. Among them, with the larger value of the $\Delta G_{*OH}$, the SACs tend to be closer to area II, implying an improved activity of 2e⁻ORR, and 2e⁻WOR. With high $\Delta G_{*OH}$ above 1.90 eV, Ni-, Cu-, Zn-, Pd-, Pt-SACs exhibit weak adsorption in area IV, which indicates the high activity of 2e⁻WOR. Besides, it can be found that axial coordination can decrease $\Delta G_{*OH}$. Furthermore, early TMs exhibit a sharp decrease of $\Delta G_{*OH}$ compared with late TMs and a moderate $\Delta G_{*OH}$ approaching or slightly exceeding 1 eV. This breaks the limitation of SACs derived from early TMs to catalyze oxygen reactions. Consequently, as shown in Fig. 3(d), there are a growing number of SACs with axial coordination exhibiting high catalytic activity towards either 4e⁻ORR, 4e⁻OER, 2e⁻ORR, or 2e⁻WOR. Therefore, the axial coordination strategy can effectively tune the catalytic activity of SACs towards oxygen-involved reactions and extend the SACs to the early TMs.

### 3.4. Catalytic activity of SACs

In this section, we discuss the correlation between the reduced adsorption energy of SACs and the improved catalytic activity towards oxygen-involved reactions. Electron transfer processes on *OOH, *OH, and *O adsorption on Mo-SAC with/without axial coordination were analyzed, and displayed in Fig. 4(a-d). Mo-SAC

displays strong adsorption of *OOH ($\Delta G_{*OOH} = -1.55$ eV), *OH ($\Delta G_{*OH} = -1.52$ eV), and *O ($\Delta G_{*O} = -2.56$ eV), phenomenally corresponding to the prolonged O–O the bond length of 2.63 Å in *OOH, short Mo–O bond lengths of 1.86 and 1.69 Å in *OH and *O. Comparably, with the additional –OH ligand in an axial direction, the adsorption ability is weakened (e.g., $\Delta G_{*OOH} = 4.18$ eV, $\Delta G_{*OH} = 1.04$ eV, and $\Delta G_{*O} = 0.70$ eV), which attributed to a shorter O–O the bond length of 1.46 Å. Additionally, the Mo–O bond lengths in *OH and *O were stretched to1.91 and 1.72 Å, respectively.

As shown in Fig. 4(b) and (d), the presence of axial coordination can reduce the electrons transferring from the central Mo site into oxygenated intermediates, which is in good agreement with the observation of the change of adsorption. In addition, considering the effect of potential by using the potential-fixed method, the axial coordination still promotes the catalytic activity (Fig. S11) [47]. Therefore, weakening the electron-donating ability of a central metal atom in SACs can tailor the adsorption ability. The Bader charge of central metals is shown in Fig. 4(e), and the plot of $\Delta G_{*OH}$ vs Bader charge is given in Fig. 5, which demonstrates that most conventional SAC configuration without axial coordination locates at the lower bound of the triangle framework. This certifies SAC configuration plays a significant role in tailoring the *OH adsorption energy of SACs. Besides, increasing the Bader charge of the TM center via axial coordination boosts the *OH adsorption energy of SACs. Increasing axial bond endows TM the highest positive charge, accordingly resulting in the weaker *OH adsorption. Furthermore, it can be observed that the SACs, located farther to the left in the periodic table, exhibit a higher charge state, indicating the role of TM species in influencing adsorption. Therefore, SAC configuration, charge state, and transition metal species were integrated into the theoretical triangular framework (**SI**) to describe the catalytic behavior of SACs.

To explore the role of TM species in tailoring the adsorption of

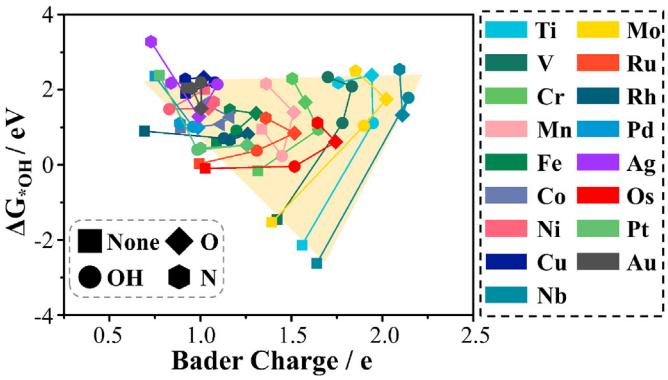


**Fig. 5.** The distribution of $\Delta G_{*OH}$ and corresponding Bader charge of active TMs in various SACs.

SACs, we further investigated the frontier *d*-orbital distribution. As displayed in Fig. S12, the coefficients of determination R-squares between spin-up (UP) *d*-band center and spin-down (DW) *d*-band center, including the projected $d_{yz^-}$, $d_{xz^-}$, $d_{xy^-}$, $d_{x^2-y^2-}$, $d_{z^2-}$ band and the full *d*-band center, are 0.78, 0.88, 0.88, 0.84, 0.88, and 0.88, respectively. Besides, their corresponding slopes are close to 1, indicating the high correlation between the spin-up (UP) d-band center and the spin-dw (DW) d-band center. It is thus reasonable to apply the single spin-up (UP) *d*-band center to describe the variation of the total *d*-band center. Furthermore, the linear fitting of $d_{yz^-}$, $d_{xz^-}$, $d_{xy^-}$, $d_{x^2-y^2-}$, $d_{z^2-}$ band center (UP) exhibited in Fig. S13 showed their R-squares of 0.88, 0.91,0.93, 0.81, and 0.94, respectively, and their corresponding formulas are shown in Table 1. These fitting results manifest that the energy level of all *d*-band centers (UP) can be expressed as a function of the energy level of $d_{z^2-}$ band center (UP). As can be seen in Fig. 6(a), with the increase of the $d_{z^2-}$ band center (UP), the order of the projected d-band is changing.

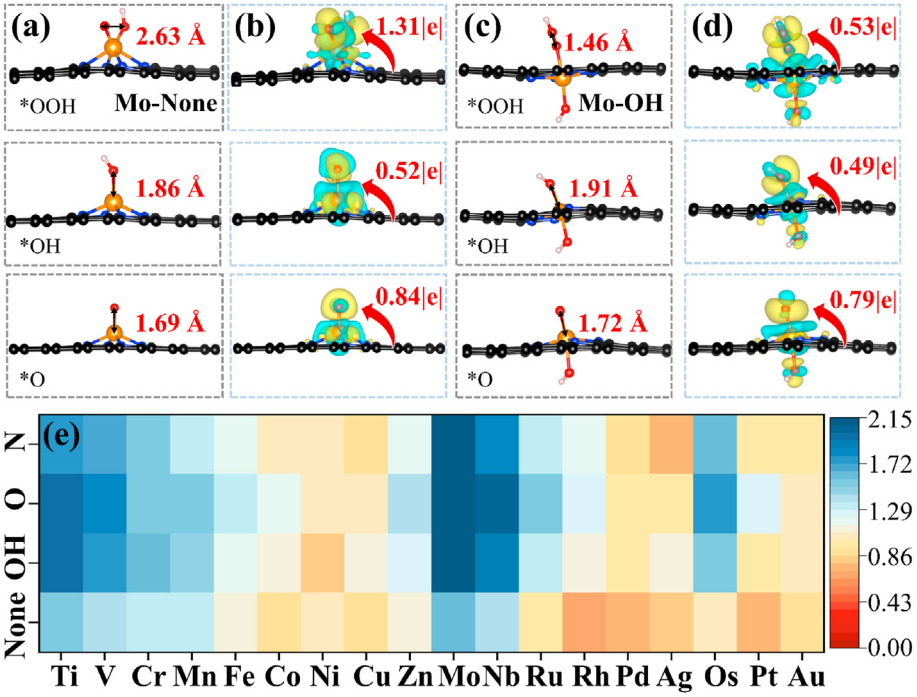


**Fig. 4.** The adsorption configuration (*OOH, *OH, and *O) on Mo (a) and Mo–OH (c), the corresponding charge difference density for Mo (b) and Mo–OH (d). The white, black, blue, red, and gold balls represent the H, C, N, O, and Mo atoms, respectively. The yellow and blue regions denote electron accumulation and depletion, respectively. The isosurface value is 0.003 e/Å$^3$. The Bader charge of active TMs in SACs (e).

**Table 1**
The linear relationship between and spin-up (UP) $d_{yz^-}$, $d_{xz^-}$, $d_{xy^-}$, $d_{x^2-y^2-}$, d-band band centers and spin-up (UP) $d_{z^2-}$ band center, where P denotes parallel lines.

| d-orbitals | Function | R [2] | Points of intersection | | | | | |
|---|---|---|---|---|---|---|---|---|
| | | | $d_{xy}$ | $d_{yz}$ | $d_{xz}$ | $d_{x^2-y^2}$ | $d_{z^2}$ | d |
| $d_{xy}$ | y = 1.09x-0.23 | 0.88 | / | −0.50 | 0.00 | P | 2.56 | P |
| $d_{yz}$ | y = 1.13x-0.21 | 0.91 | −0.50 | / | P | 9.00 | 1.62 | 3.50 |
| $d_{xz}$ | y = 1.14x-0.23 | 0.93 | 0.00 | P | / | 7.60 | 1.64 | 5.20 |
| $d_{x^2-y^2}$ | y = 1.09x-0.15 | 0.81 | P | 9.00 | 7.60 | / | −1.67 | P |
| $d_{z^2}$ | y = x | / | 2.56 | 1.62 | 1.64 | −1.67 | / | 0.78 |
| d | y = 1.09x-0.07 | 0.94 | P | 3.50 | 5.20 | P | 0.78 | / |

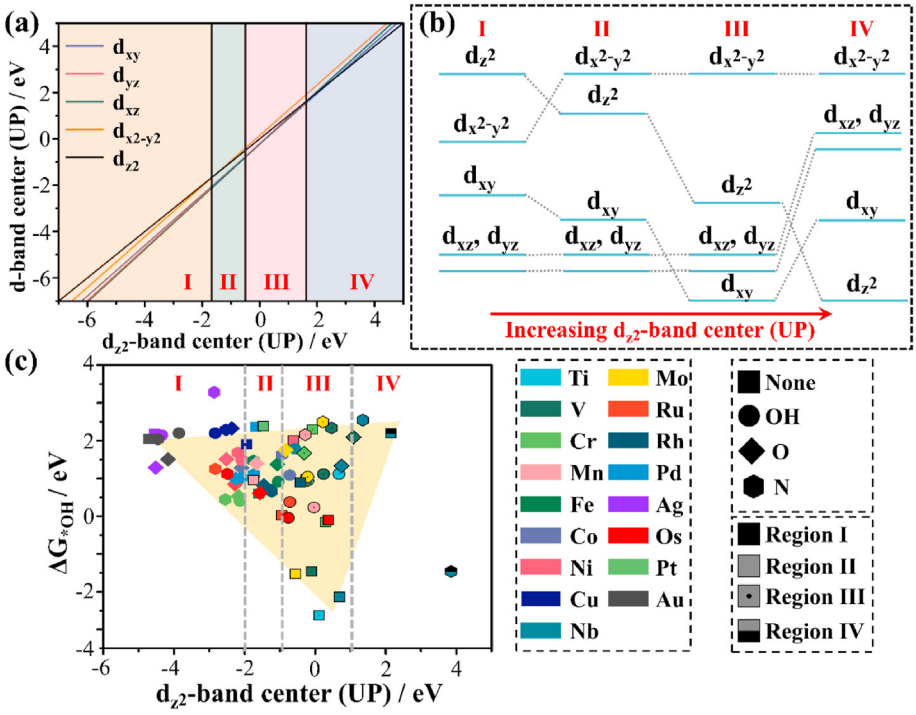


**Fig. 6.** The linear relationship between and spin-up (UP) $d_{yz^-}$, $d_{xz^-}$, $d_{xy^-}$, $d_{x^2-y^2-}$, $d_{z^2-}$ band centers and spin-up (UP) $d_{z^2-}$ band center (a). Orbital splitting pattern along increasing spin-up (UP) $d_{z^2-}$ band center (b). The distribution of $\Delta G_{*OH}$ and corresponding spin-up (UP) $d_{z^2-}$ band center of active TMs in various SACs (c).

Based on the points of intersection listed in Table 1, we can divide Fig. 6(a) into four areas, and each area corresponds to a *d*-orbital splitting shown in Fig. 6(b).

As shown in Fig. 6(a) and (b), with the increase of the $d_{z^2-}$ band center (UP), the relative order of $d_{z^2-}$ orbitals downshift, while $d_{xz-}$ and $d_{yz-}$ orbitals upshift to a relatively higher order. As reported previously, decreasing d-electrons can induce the upshift of the d-band center [48–50]. Such upshift will lead to the reordering of the $d_{z2}$-orbital (downshift) and $d_{xz-}$ and $d_{yz-}$ orbitals (upshift) in Fig. 6(b). It drives the $d_{z^2-}$ orbital approaching the Fermi level and becoming a good electron donor, whereas the $d_{xz-}$, $d_{yz-}$ orbitals becoming good electron acceptors. Such change can strengthen the interaction between SACs and the adsorbates since the three *d*-orbitals are mainly involved in the bonding with adsorbates [51]. Therefore, the early TM-derived SACs, with fewer electrons in *d*-orbitals, have the weak adsorption ability of SACs. We then divided the framework in Fig. 6(c) into 4 areas. There are various cases of 3*d*-orbital splitting in each area. In conventional SACs, Cu, Ag, and Au belong to area I, and most Mn, Fe-, Co-, Ni-, Ru-, Pd-, and Pt-derived SACs are in area II, while Ti-, V— Cr-, Nb-, Mo-, Rh-, and Os-derived SACs located at area III. It is worth mentioning that part of SACs, such as Ni, exists in two areas because axial coordination can regulate not only the charge state of metal sites but also the energy level distribution of 3*d*-orbitals through orbital interaction [52–54]. Therefore, the number of d-electrons in the 3d-orbital of SACs, determining the 3d-orbital splitting, further affects the adsorption behavior of SACs. Therefore, a theoretical framework plotted in Fig. 6, combining TM species, charge states, and SAC configurations can be employed to describe the adsorption of SACs and catalytic activity toward oxygen-involved reaction.

## 4. Conclusions

In this work, we investigated the catalytic activity of a single atomic catalyst (SAC) with axial coordination towards oxygen-involving reaction, including $4e^-/2e^-$ORR, $4e^-$OER, and $2e^-$WOR by density functional theory calculations. With the presence of axial coordination (-OH, =O, and ≡N), SACs, even early TMs-derived SACs, can exhibit high catalytic activity towards four oxygen-involved reactions. The accurate scaling relation confirmed weakening the adsorption ability can improve the catalytic activity towards different oxygen reactions. More importantly, a theoretical

framework of SAC configuration, transition metal (TM) species, and TM charge states have been established to describe the adsorption ability of SACs. This work offers an intrinsic landscape to explore the catalytic activity of SACs, providing rational guidelines for designing high-performance SACs.

## Author Contributions

**Zhang Chengyi**: Conceptualization, Software, Writing- Original draft preparation. **Dai Yuhang:** Conceptualization. **Sun Qi:** Supervision, Data Curation. **Ye Chumei:** Visualization. **Lu Ruihu:** Conceptualization, Software, Formal analysis. **Zhou Yazhou:** Validation. **Zhao Yan:** Funding acquisition, Project administration, Supervision

## Declaration of competing interest

The authors declare that they have no known competing financial interests or personal relationships that could have appeared to influence the work reported in this paper.

## Acknowledgments

The work in this paper was supported in part by the Foshan Xianhu Laboratory of the Advanced Energy Science and Technology Guangdong Laboratory (XHT2020-003) and by the Key R&D program of Hubei (2021BAA173).

## Appendix A. Supplementary data

Supplementary data to this article can be found online at https://doi.org/10.1016/j.mtadv.2022.100280.

## References

[1] S. Yang, A. Verdaguer-Casadevall, L. Arnarson, L. Silvio, V. Colic, R. Frydendal, J. Rossmeisl, I. Chorkendorff, I.E.L. Stephens, Toward the decentralized electrochemical production of $H_2O_2$: a focus on the catalysis, ACS Catal. 8 (2018) 4064–4081.

[2] S. Siahrostami, A. Verdaguer-Casadevall, M. Karamad, D. Deiana, P. Malacrida, B. Wickman, M. Escudero-Escribano, E.A. Paoli, R. Frydendal, T.W. Hansen, I. Chorkendorff, I.E. Stephens, J. Rossmeisl, Enabling direct $H_2O_2$ production through rational electrocatalyst design, Nat. Mater. 12 (2013) 1137–1143.

[3] Zaman, S.; Huang, L.; Douka, A. I.; Yang, H.; You, B.; Xia, B. Y., Oxygen reduction electrocatalysts toward practical fuel cells: progress and perspectives. Angew Chem. Int. Ed. Engl. 60 (2021), 17832-17852.

[4] D. Wu, X. Shen, Y. Pan, L. Yao, Z. Peng, Platinum alloy catalysts for oxygen reduction reaction: advances, challenges and perspectives, ChemNanoMat 6 (2019) 32–41.

[5] Y.C. Liu, Y. Li, H.Y. Kang, T. Jin, L.F. Jiao, Design, synthesis, and energy-related applications of metal sulfides, Mater. Horiz. 3 (2016) 402–421.

[6] Z.H. Pu, T.T. Liu, I.S. Amiinu, R.L. Cheng, P.Y. Wang, C.T. Zhang, P.X. Ji, W.H. Hu, J. Liu, S.C. Mu, Transition-metal phosphides: activity origin, energy-related electrocatalysis applications, and synthetic strategies, Adv. Funct. Mater. 30 (2020), 2004009.

[7] D.A. Kuznetsov, B. Han, Y. Yu, R.R. Rao, J. Hwang, Y. Roman-Leshkov, Y. Shao-Horn, Tuning redox transitions via inductive effect in metal oxides and complexes, and implications in oxygen electrocatalysis, Joule 2 (2018) 225–244.

[8] S. Gupta, W. Kellogg, H. Xu, X. Liu, J. Cho, G. Wu, Bifunctional perovskite oxide catalysts for oxygen reduction and evolution in alkaline media, Chem. Asian J. 11 (2016) 10–21.

[9] X. Long, Z.L. Wang, S. Xiao, Y.M. An, S.H. Yang, Transition metal based layered double hydroxides tailored for energy conversion and storage, Mater. Today 19 (2016) 213–226.

[10] R.G. Ma, G.X. Lin, Y. Zhou, Q. Liu, T. Zhang, G.C. Shan, M.H. Yang, J.C. Wang, A review of oxygen reduction mechanisms for metal-free carbon-based electrocatalysts, npj Comput. Mater. 5 (2019) 78.

[11] X.Q. Wang, Z.J. Li, Y.T. Qu, T.W. Yuan, W.Y. Wang, Y. Wu, Y.D. Li, Review of metal catalysts for oxygen reduction reaction: from nanoscale engineering to atomic design, Chem 5 (2019) 1486–1511.

[12] C.L. Zhang, X.C. Shen, Y.B. Pan, Z.M. Peng, A review of Pt-based electrocatalysts for oxygen reduction reaction, Front. Energy 11 (2017) 268–285.

[13] Zhao, C. X.; Li, B. Q.; Liu, J. N.; Zhang, Q., Intrinsic electrocatalytic activity regulation of M-N-C single-atom catalysts for the oxygen reduction reaction. Angew Chem. Int. Ed. Engl. 60 (2021), 4448-4463.

[14] J. Wu, L. Xiong, B. Zhao, M. Liu, L. Huang, Densely populated single atom catalysts, Small Methods 4 (2019), 1900540.

[15] C. Zhu, S. Fu, Q. Shi, D. Du, Y. Lin, Single-atom electrocatalysts, Angew Chem. Int. Ed. Engl. 56 (2017) 13944–13960.

[16] R.H. Lu, C.X. Quan, C.Y. Zhang, Q. He, X.B. Liao, Z.Y. Wang, Y. Zhao, Establishing a theoretical insight for penta-coordinated iron-nitrogen-carbon catalysts toward oxygen reaction, Nano Res. 15 (2022) 6067–6075, https://doi.org/10.1007/s12274-022-4318-2. In this issue.

[17] R. Ma, G. Lin, Q. Ju, W. Tang, G. Chen, Z. Chen, Q. Liu, M. Yang, Y. Lu, J. Wang, Edge-sited Fe-$N_4$ atomic species improve oxygen reduction activity via boosting $O_2$ dissociation, Appl. Catal., B 265 (2020), 118593.

[18] J.Y. Feng, R.S. Cai, E. Magliocca, H. Luo, L. Higgins, G.L.F. Romario, X.Q. Liang, A. Pedersen, Z. Xu, Z.Y. Guo, A. Periasamy, D. Brett, T.S. Miller, S.J. Haigh, B. Mishra, M.M. Titirici, Iron, nitrogen Co-doped carbon spheres as low cost, scalable electrocatalysts for the oxygen reduction reaction, Adv. Funct. Mater. 31 (2021), 2102974.

[19] F. Li, G.F. Han, Y. Bu, H.J. Noh, J.P. Jeon, T.J. Shin, S.J. Kim, Y. Wu, H.Y. Jeong, Z. Fu, Y. Lu, J.B. Baek, Revealing isolated M-$N_3C_1$ active sites for efficient collaborative oxygen reduction catalysis, Angew Chem. Int. Ed. Engl. 59 (2020) 23678–23683.

[20] H. Shang, X. Zhou, J. Dong, A. Li, X. Zhao, Q. Liu, Y. Lin, J. Pei, Z. Li, Z. Jiang, D. Zhou, L. Zheng, Y. Wang, J. Zhou, Z. Yang, R. Cao, R. Sarangi, T. Sun, X. Yang, X. Zheng, W. Yan, Z. Zhuang, J. Li, W. Chen, D. Wang, J. Zhang, Y. Li, Engineering unsymmetrically coordinated Cu-$S_1N_3$ single atom sites with enhanced oxygen reduction activity, Nat. Commun. 11 (2020) 3049.

[21] Zhang, S.; Xue, H.; Li, W. L.; Sun, J.; Guo, N.; Song, T.; Dong, H.; Zhang, J.; Ge, X.; Zhang, W.; Wang, Q., Constructing precise coordination of nickel active sites on hierarchical porous carbon framework for superior oxygen reduction. Small 17 (2021), 2102125.

[22] C. Zhu, Q. Shi, B.Z. Xu, S. Fu, G. Wan, C. Yang, S. Yao, J. Song, H. Zhou, D. Du, S.P. Beckman, D. Su, Y. Lin, Hierarchically porous M–N–C (M = Co and Fe) single-atom electrocatalysts with robust MNx active moieties enable enhanced ORR performance, Adv. Energy Mater. 8 (2018), 1801956.

[23] A. Zitolo, N. Ranjbar-Sahraie, T. Mineva, J. Li, Q. Jia, S. Stamatin, G.F. Harrington, S.M. Lyth, P. Krtil, S. Mukerjee, E. Fonda, F. Jaouen, Identification of catalytic sites in cobalt-nitrogen-carbon materials for the oxygen reduction reaction, Nat. Commun. 8 (2017) 957.

[24] Y. He, S. Liu, C. Priest, Q. Shi, G. Wu, Atomically dispersed metal-nitrogen-carbon catalysts for fuel cells: advances in catalyst design, electrode performance, and durability improvement, Chem. Soc. Rev. 49 (2020) 3484–3524.

[25] Liu, J.; Gong, Z.; Yan, M.; He, G.; Gong, H.; Ye, G.; Fei, H., Electronic structure regulation of single-atom catalysts for electrochemical oxygen reduction to H2 O2. Small 18 (2022), 2103824.

[26] Wang, Y.; Shao, M., Theoretical screening of transition metal–$N_4$-doped graphene for electroreduction of nitrate. ACS Catal.. 12 (2022), 5407-5415.

[27] W. Kohn, L.J. Sham, Self-consistent equations including exchange and correlation effects, Phys. Rev. 140 (1965) A1133–A1138.

[28] G. Kresse, J. Hafner, Ab initio molecular dynamics for liquid metals, Phys. Rev. B Condens. Matter 47 (1993) 558–561.

[29] G. Kresse, J. Hafner, Ab initio molecular-dynamics simulation of the liquid-metal-amorphous-semiconductor transition in germanium, Phys. Rev. B Condens. Matter 49 (1994) 14251–14269.

[30] J.P. Perdew, K. Burke, M. Ernzerhof, Generalized gradient approximation made simple, Phys. Rev. Lett. 77 (1996) 3865–3868.

[31] P.E. Blochl, Projector augmented-wave method, Phys. Rev. B Condens. Matter 50 (1994) 17953–17979.

[32] S. Grimme, J. Antony, S. Ehrlich, H. Krieg, A consistent and accurate ab initio parametrization of density functional dispersion correction (DFT-D) for the 94 elements H-Pu, J. Chem. Phys. 132 (2010), 154104.

[33] H.J. Monkhorst, J.D. Pack, Special points for Brillouin-zone integrations, Phys. Rev. B 13 (1976) 5188–5192.

[34] K. Momma, F. Izumi, VESTA: a three-dimensional visualization system for electronic and structural analysis, J. Appl. Crystallogr. 41 (2008) 653–658.

[35] J.K. Nørskov, J. Rossmeisl, A. Logadottir, L. Lindqvist, J.R. Kitchin, T. Bligaard, H. Jónsson, Origin of the overpotential for oxygen reduction at a fuel-cell cathode, J. Phys. Chem. B 108 (2004) 17886–17892.

[36] J.K. Nørskov, T. Bligaard, A. Logadottir, J.R. Kitchin, J.G. Chen, S. Pandelov, U. Stimming, Trends in the exchange current for hydrogen evolution, J. Electrochem. Soc. 152 (2005) J23–J26.

[37] J. Haskins, A. Kinaci, C. Sevik, H. Sevincli, G. Cuniberti, T. Cagin, Control of thermal and electronic transport in defect-engineered graphene nanoribbons, ACS Nano 5 (2011) 3779–3787.

[38] Y. Chen, S. Ji, S. Zhao, W. Chen, J. Dong, W.C. Cheong, R. Shen, X. Wen, L. Zheng, A.I. Rykov, S. Cai, H. Tang, Z. Zhuang, C. Chen, Q. Peng, D. Wang, Y. Li, Enhanced oxygen reduction with single-atomic-site iron catalysts for a zinc-air battery and hydrogen-air fuel cell, Nat. Commun. 9 (2018) 5422.

[39] Liu, K.; Fu, J.; Lin, Y.; Luo, T.; Ni, G.; Li, H.; Lin, Z.; Liu, M., Insights into the activity of single-atom Fe-N-C catalysts for oxygen reduction reaction. Nat. Commun. 13 (2022), 2075.

[40] C.Z. Wan, X.F. Duan, Y. Huang, Molecular design of single-atom catalysts for oxygen reduction reaction, Adv. Energy Mater. 10 (2020), 1903815.

[41] Anantharaj, S.; Pitchaimuthu, S.; Noda, S., A review on recent developments in electrochemical hydrogen peroxide synthesis with a critical assessment of

perspectives and strategies. Adv. Colloid Interface Sci. 287 (2021), 102331.
[42] Y.C. Wang, Y. Liu, W. Liu, J. Wu, Q. Li, Q.G. Feng, Z.Y. Chen, X. Xiong, D.S. Wang, Y.P. Lei, Regulating the coordination structure of metal single atoms for efficient electrocatalytic $CO_2$ reduction, Energy Environ. Sci. 13 (2020) 4609–4624.
[43] I.C. Man, H.Y. Su, F. Calle-Vallejo, H.A. Hansen, J.I. Martinez, N.G. Inoglu, J. Kitchin, T.F. Jaramillo, J.K. Norskov, J. Rossmeisl, Universality in oxygen evolution electrocatalysis on oxide surfaces, ChemCatChem 3 (2011) 1159–1165.
[44] G. Zhu, F. Liu, Y. Wang, Z. Wei, W. Wang, Systematic exploration of N,C coordination effects on the ORR performance of Mn-Nx doped graphene catalysts based on DFT calculations, Phys. Chem. Chem. Phys. 21 (2019) 12826–12836.
[45] S. Wannakao, T. Maihom, K. Kongpatpanich, J. Limtrakul, V. Promarak, Halogen substitutions leading to enhanced oxygen evolution and oxygen reduction reactions in metalloporphyrin frameworks, Phys. Chem. Chem. Phys. 19 (2017) 29540–29548.
[46] E. Jung, H. Shin, B.H. Lee, V. Efremov, S. Lee, H.S. Lee, J. Kim, W. Hooch Antink, S. Park, K.S. Lee, S.P. Cho, J.S. Yoo, Y.E. Sung, T. Hyeon, Atomic-level tuning of Co-N-C catalyst for high-performance electrochemical $H_2O_2$ production, Nat. Mater. 19 (2020) 436–442.
[47] G. Gao, L.-W. Wang, Substantial potential effects on single-atom catalysts for the oxygen evolution reaction simulated via a fixed-potential method, J. Catal. 391 (2020) 530–538.
[48] X. Wang, H. Niu, Y. Liu, C. Shao, J. Robertson, Z. Zhang, Y. Guo, Theoretical investigation on graphene-supported single-atom catalysts for electrochemical $CO_2$ reduction, Catal. Sci. Technol. 10 (2020) 8465–8472.
[49] W. Yang, S. Xu, K. Ma, C. Wu, I.D. Gates, X. Ding, W. Meng, Z. Gao, Geometric structures, electronic characteristics, stabilities, catalytic activities, and descriptors of graphene-based single-atom catalysts, Nano Mater. Sci. 2 (2020) 120–131.
[50] T.D. Spivey, A. Holewinski, Selective interactions between free-atom-like d-states in single-atom alloy catalysts and near-frontier molecular orbitals, J. Am. Chem. Soc. 143 (2021) 11897–11902.
[51] Y. Sun, S. Sun, H. Yang, S. Xi, J. Gracia, Z.J. Xu, Spin-Related electron transfer and orbital interactions in oxygen electrocatalysis, Adv. Mater. 32 (2020) 2003297–2003405.
[52] Y. Lin, P. Liu, E. Velasco, G. Yao, Z. Tian, L. Zhang, L. Chen, Fabricating single-atom catalysts from chelating metal in open frameworks, Adv. Mater. 31 (2019), 1808193.
[53] Y.H. Han, Y.G. Wang, R.R. Xu, W.X. Chen, L.R. Zheng, A.J. Han, Y.Q. Zhu, J. Zhang, H.B. Zhang, J. Luo, C. Chen, Q. Peng, D.S. Wang, Y.D. Li, Electronic structure engineering to boost oxygen reduction activity by controlling the coordination of the central metal, Energy Environ. Sci. 11 (2018) 2348–2352.
[54] Chen, Z.; Huang, A.; Yu, K.; Cui, T.; Zhuang, Z.; Liu, S.; Li, J.; Tu, R.; Sun, K.; Tan, X.; Zhang, J.; Liu, D.; Zhang, Y.; Jiang, P.; Pan, Y.; Chen, C.; Peng, Q.; Li, Y., $Fe_1N_4$–$O_1$ site with axial Fe–O coordination for highly selective $CO_2$ reduction over a wide potential range. Energy Environ. Sci. 14 (2021), 3430-3437.